OXFORD

Unlocking precision gene therapy: harnessing AAV tropism with nanobody swapping at capsid hotspots

Mareike D. Hoffmann [1,*], **Joseph P. Gallant**[2], **Aaron M. LeBeau**[2,3] **and Daniel Schmidt** [1,*]

[1]Department of Genetics, Cell Biology & Development, University of Minnesota, Minneapolis, MN 55455, USA
[2]Department of Pathology and Laboratory Medicine, University of Wisconsin School of Medicine and Public Health, Madison, WI 53792, USA
[3]Department of Radiology, University of Wisconsin School of Medicine and Public Health, Madison, WI 53792, USA
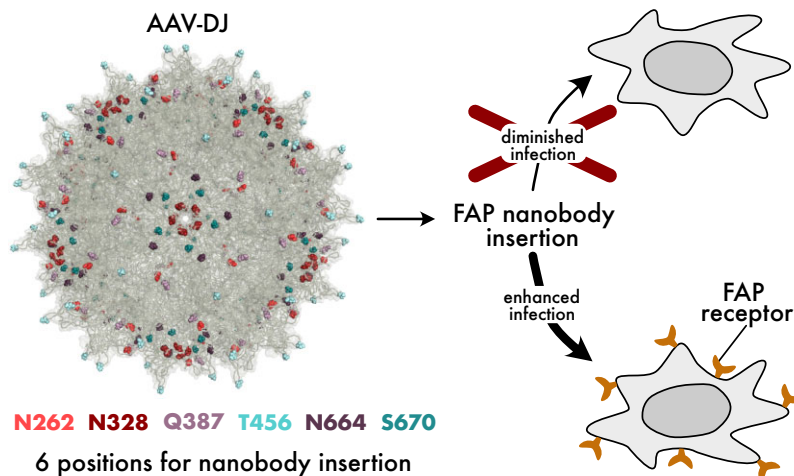
*To whom correspondence should be addressed. Tel: +1 612 625 1180; Email: schmida@umn.edu
Correspondence may also be addressed to Mareike D. Hoffmann. Tel: +1 612 625 2157; Email: hoff1570@umn.edu

Abstract

Adeno-associated virus (AAV) has been remarkably successful in the clinic, but its broad tropism is a practical limitation of precision gene therapy. A promising path to engineer AAV tropism is the addition of binding domains to the AAV capsid that recognize cell surface markers present on a targeted cell type. We have recently identified two previously unexplored capsid regions near the 2/5-fold wall and 5-fold pore of the AAV capsid that are amenable to insertion of larger protein domains, including nanobodies. Here, we demonstrate that these hotspots facilitate AAV tropism switching through simple nanobody replacement without extensive optimization in both VP1 and VP2. Our data suggest that engineering VP2 is the preferred path for maintaining both virus production yield and infectivity. We demonstrate highly specific targeting of human cancer cells expressing fibroblast activating protein (FAP). Furthermore, we found that the combination of FAP nanobody insertion plus ablation of the heparin binding domain can reduce off-target infection to a minimum, while maintaining a strong infection of FAP receptor-positive cells. Taken together, our study shows that nanobody swapping at multiple capsid locations is a viable strategy for nanobody-directed cell-specific AAV targeting.

Graphical abstract

AAV-DJ

N262 N328 Q387 T456 N664 S670

6 positions for nanobody insertion

FAP nanobody insertion

diminished infection

enhanced infection

FAP receptor

Introduction

Adeno-associated virus (AAV) is a compact 25-nm virus known for its favorable clinical characteristics, such as low pathogenicity and the ability to induce long-term expression in both dividing and nondividing cells. These features make it a promising candidate for applications in gene and cell therapy [reviewed in (1)]. Its single-stranded DNA (ssDNA) genome, spanning 4.7 kb, encodes two genes, *rep* and *cap*, flanked by inverted terminal repeats. The *cap* gene produces three viral proteins (VP1, VP2 and VP3) from the same open reading frame. VP2 is an N-terminal truncated version of VP1, and VP3 is a further truncated version of VP2 (2,3). The capsid, formed by 60 VP monomers, exhibits an icosahedral structure with an average ratio of 1:1:10 for VP1, VP2 and VP3, respectively (4–6).

The capsid's distinctive features include a protruding, cylindrical pore at the 5-fold interface, a valley extending toward the 2-fold interface around the pore and protrusions at the

3-fold interface, which play a crucial role in mediating target cell receptor binding (7). Despite high conservation in the overall structure and topology across serotypes, structural analyses have identified nine variable regions (VR1–9) on the capsid surface (8). VR4 and VR8 have been particularly targeted in AAV capsid engineering to evade neutralizing antibody binding (9) and redirect viral tropism (10–15).

While VR8 has been predominantly utilized for peptide insertions, a library screen by Judd *et al.* (16) revealed that VR4 can accommodate the fluorescent protein mCherry. After this discovery, various protein domains with retargeting capabilities, including DARPins (17), HUH-tags (18) and nanobodies (19,20), were successfully incorporated into VR4. Nanobodies, originating from camelids and characterized by their small size (15 kDa), specificity, stability and ability to serve as targeting ligands for chemotherapy drugs, radionuclides or toxins (21), stand out among these options. Therefore, there is considerable interest in optimizing the incorporation of nanobodies into the AAV capsid to enhance cell-type-specific AAV targeting.

In a previous work, we have performed a domain insertion library screen by incorporating domains with retargeting abilities, including a GFP nanobody, in between every two amino acid residues of VP1 protein of AAV-DJ (22). We demonstrated that nanobody insertions are tolerated not only in the tip of the 3-fold protrusion (VR4), but also at several positions lining the 2-fold valley as well as the 5-fold interface of an AAV capsid. While insertion of a GFP nanobody into AAV increased infectivity toward cells expressing GFP on their cell surface, it was unclear whether this nanobody-mediated retargeting generalizes to different nanobodies, implying modularity, or whether any optimization is required to achieve high infection specificity.

To address these questions, we selected seven positions at the 2/5-fold wall and 5-fold interface alongside the benchmark insertion position in VR4. Insertions were made into either the VP1 or VP2 protein of AAV-DJ with two different types of linkers. We chose AAV-DJ as a test bed for consistency with our previous domain insertional screen (22). With an eye toward clinically relevant AAV retargeting, we chose a nanobody targeting fibroblast activating protein (FAP), which has emerged as a promising cancer target in recent years (23–25). While most of our FAP nanobody insertion variants have weaker infection efficacy on cells lacking the FAP receptor (i.e. off-target cells), most of the variants (six out of the eight positions tested) surpassed the AAV-DJ control in FAP receptor-positive ('on-target') cells with a specificity gain of up to 18-fold for the best variant: VP2-N262 with asymmetric linkers. When we combined FAP nanobody insertion with ablation of the heparin binding domain (HBD), we could maintain infection potency of on-target cells, while reducing off-target infection of hepatocytes to a minimum. These findings reinforce the feasibility of nanobody-mediated AAV targeting for cell and gene therapy applications.

Materials and methods

Cloning

Oligos and gBlocks were obtained from IDT, restriction enzymes and T4 DNA ligase were obtained from NEB and polymerase chain reactions (PCRs) were done using the PrimeSTAR Max DNA polymerase from Takara Bio. PCR products were purified using the DNA Clean & Concentrator-5 Kit (Zymo Research) or the Zymoclean Gel DNA Extraction Kit (Zymo Research) if PCR products were analyzed on 1% Tris-acetate-EDTA agarose gels. Post-cloning, plasmids were transformed into NEB® Stable Competent *Escherichia coli* cells, before plating on Luria-Bertani broth plates containing carbenicillin at a concentration of 100 μg/ml. Plasmids were isolated using the Zyppy Plasmid Miniprep Kit (Zymo Research), according to the manufacturer's instructions. All plasmids used in this study are listed in Supplementary Table S1. For the cloning of the FAP nanobody insertion variants, the BsmBI restriction site was eliminated from the plasmid containing the rep2–capDJ (AAV-DJ) gene sequences by introducing a silent mutation using mutagenesis PCR at position D178 of the capDJ gene. The plasmids DJ-VP1 and DJ-VP2 were obtained by mutating the start codons for VP2/3 (T138A, M203K, M211L, M235L) and VP1/3 (M1K, M203K, M211L, M235L), respectively. Then, for the AAV production, obligatory plasmids complementing the missing VPs, DJ-VP2/3 and DJ-VP1/3, were cloned similarly by mutating the start codons for VP1 (M1K) and VP2 (T138A), respectively. FAP or GFP nanobody insertion plasmids were generated using golden gate assembly (26) and the BsmBI restriction enzyme. FAP (Supplementary Figure S1) and GFP nanobody (27) sequences were human codon-optimized and ordered as gBlocks with either symmetric or asymmetric linkers. Nanobody and linker sequences are given in Supplementary Figure S1. Point mutations R587A and R590A (HBD) were introduced by site-directed mutagenesis. Post-cloning, sequences were verified by Plasmid-EZ sequencing (Azenta Life Sciences).

Tissue culture

The prostate cancer cell lines CWR-R1-enzalutamide-resistant/luciferase+ (stably expressing a firefly luciferase), in this manuscript referred to as R1 cells, and CWR-R1-enzalutamide-resistant/luciferase plus FAP (additionally expressing a human FAP receptor), in this manuscript referred to as R1-FAP cells, were provided by the LeBeau lab at the University of Wisconsin (28). Both cell lines and 293AAV cells (Cell Biolabs) were cultured in Dulbecco's modified Eagle medium (Gibco) supplemented with 10% fetal bovine serum (FBS; Gibco), 4.5 g/l D-glucose, L-glutamine, 110 mg/l sodium pyruvate and 100 U/ml penicillin/100 μg/ml streptomycin (Gibco). The medium for R1-FAP cells was additionally supplemented with 3 μg/ml puromycin (ApexBio Technology). SK-MEL-24 and HepG2 cells were cultured in Eagle's minimum essential medium (ATCC) supplemented with 110 mg/l sodium pyruvate, and 100 U/ml penicillin/100 μg/ml streptomycin (Gibco) and 15% or 10% FBS, respectively. Cells were kept in a humidified incubator at 37°C and 5% CO_2 and passaged every 2–4 days when reaching a confluence of 70–80%.

AAV crude lysate production

293AAV cells were seeded into six-well plates at a density of 500 000 cells per well. Twenty-four hours later, cells were transfected with 2.5 μg DNA using polyethylenimine and an equimolar ratio of the plasmids necessary for the respective AAV production: (i) an Adenohelper plasmid; (ii) a nanoLuciferase encoding plasmid; (iii) a plasmid encoding rep2 and capDJ with start codons of either only VP1 or only VP2, but

with a FAP nanobody insertion; and (iv) a plasmid encoding rep2 and capDJ encoding the VP proteins needed for complementation. Three days post-transfection, cells were harvested by flushing off the cells by pipetting and spun down for 5 min at $400 \times g$. Cells were resuspended in phosphate-buffered saline (PBS, pH 7.4; Gibco) and then subjected to five freeze and thaw cycles by alternating between liquid nitrogen and a 37°C water bath. Cell debris was pelleted by centrifugation at $17\,000 \times g$ at 4°C for 10 min. The supernatant containing the AAV particles was stored at −20°C until use.

Purified AAV production

293AAV cells were seeded into 15-cm plates at a density of 12 million cells per plate and 10 plates in total were used per production. Twenty-four hours post-seeding, transfection was performed as described for the crude lysate production, but with a total amount of 47 µg DNA per plate. Seventy-two hours post-transfection, cells were harvested and AAV purified by published iodixanol gradient purification protocols (29,30) and as previously described by us (22).

Quantitative PCR

Production titers of crude lysate samples were determined as follows. Two microliters of the crude lysates were mixed with PBS, supplemented with 2 mM $MgCl_2$, and 0.1 µl ultrapure Benzonase Nuclease (Sigma–Aldrich) was added. Samples were incubated at 37°C for 30 min to digest DNA that was not protected by AAV capsids. Next, 5 µl $10\times$ Proteinase K buffer (100 nM Tris–HCl, pH 8.0, 10 mM ethylenediaminetetraacetic acid and 10 % sodium dodecyl sulfate) and 1 µl Proteinase K (20 mg/ml; Zymo Research) were added inhibiting the Benzonase and digesting proteins including the AAV capsid to free the ssDNA. Afterward, samples were incubated for 20 min at 50°C, followed by heat inactivation of the Proteinase K for 5 min at 95°C. The viral ssDNA was purified using the DNA Clean & Concentrator-5 Kit (Zymo Research), according to the manufacturer's instructions for ssDNA purification. All samples were diluted 1:500 in H_2O prior to quantitative PCR (qPCR), which was run using a QuantStudio5 Real-Time PCR System (Applied Biosystems) and by using the PowerUp SYBR Green Master Mix (Applied Biosystems), following the manufacturer's instructions. A primer set binding within the CMV enhancer (forward: AACGCCAATAGGGACTTTCC; reverse: GGGCGTACTTGGCATATGAT) of the transgene expression cassette was used. To calculate the viral titer in vg/ml, a plasmid standard at a known concentration also containing a CMV enhancer was used. For quantification of gradient-purified AAV, the Benzonase digest step was skipped.

Luciferase assay

R1, R1-FAP and HepG2 cells were seeded into 96-well plates at a density of 12 500 cells per well, while SK-MEL-24 cells were plated at a density of 10 000 cells per well. The next day, the medium was replaced, and cells were transduced at the indicated multiplicity of infection (MOI) with AAV crude lysates. Forty-eight hours post-transduction, the medium was aspirated, cells were washed with 100 µl PBS (pH 7.4, Gibco) per well, and then 25 µl PBS and 25 µl of the Nano-Glo® Luciferase Assay System reagent (Promega) were added. Cells were incubated for 15 min at room temperature on a shaker at 600 rpm. Afterward, the suspension was mixed by pipetting

up and down before 20 µl was transferred into a white 96-well F-bottom plate (Corning). Luminescence was measured using an Infinite F200 PRO plate reader (Tecan) by using an integration time of 100 ms. Note that the firefly luciferase (stably expressed by the cell line) and the NanoLuc (delivered as transgene by the AAV) use fully orthogonal substrates, D-luciferin and furimazine, respectively (31), meaning that the integrated firefly luciferase does not contribute to measured signal. Luciferase assays were conducted with three technical replicates per sample.

Flow cytometry

To analyze FAP expression, 2 million R1, R1-FAP, SK-MEL-24 and HepG2 cells were detached with Accutase solution (Sigma–Aldrich), collected in a 15-ml conical tube and spun down at $400 \times g$ for 3 min at 4°C. The cell pellets were resuspended in 1 ml cold flow buffer (PBS supplemented with 5% FBS and 0.1% sodium azide). Next, the cell suspensions were split into two halves and transferred into cold microcentrifuge tubes and washed two more times with cold 500 µl flow buffer. The unstained samples remained in flow buffer, while the stained samples were resuspended in flow buffer supplemented with the primary antibody (anti-FAP human B12) (24) at a dilution of 1:500. Incubation was done for 1 h at 4°C in an end-over-end rotator. Both cell batches, unstained and stained, were washed three times in cold flow buffer and then the secondary antibody (Goat Anti-Human IgG H + L Cross-Adsorbed Secondary Antibody, Alexa Fluor™ 488, Thermo Fisher Scientific) at a dilution of 1:500 was added. The incubation of the secondary antibody was done for 1 h at 4°C in an end-over-end rotator. Cells were washed another three times in cold flow buffer before passing through a 35-µm cell strainer to avoid cell clumps. Flow cytometry was done on a SONY SH800 flow sorter equipped with a 488-nm laser. Gates for the whole-cell population and single-cell population were adjusted to the different cell types tested. At least 20 000 single-cell events were recorded for each sample.

Pulldown assay

All steps of the pulldown assay were performed with ice-cold solutions and incubations were done at 4°C, unless otherwise stated. First, 20 µl of Dynabeads™ His-Tag Isolation & Pulldown bead slurry (Thermo Fisher Scientific) was washed four times with 0.7 ml washing buffer (300 mM NaCl, 50 mM $NaHPO_4$, 0.01% Tween 20, pH 8.0) to equilibrate the beads. Next, the beads were resuspended in 695 µl wash buffer and 5 µl recombinant FAP protein with a C-terminal His-tag (Abcam) was added. To allow for binding of the FAP protein to the beads, samples were incubated for 1 h in an end-over-end rotator. Next, samples were washed four times with 0.7 ml wash buffer by thoroughly pipetting up and down to eliminate unbound FAP protein. The beads were then resuspended in 700 µl wash buffer and $\sim 2 \times 10^{10}$ vg of iodixanol gradient-purified AAV was added. Samples were incubated for another hour in an end-over-end rotator. Samples were washed again four times with 0.7 ml wash buffer before they were resuspended in 50 µl PBS. To extract the ssDNA payload from the AAV particles bound to the beads, 5.5 µl Proteinase K buffer and 1 µl Proteinase K were added and samples incubated for 20 min at 50°C. Proteinase K was then heat inactivated at 95°C for 10 min before the ssDNA was extracted using the DNA Clean & Concentrator-5 Kit. AAV samples from before

and after the pulldown were then quantified using qPCR as described earlier. Percentage of bound AAV was calculated and normalized to the AAV-DJ control.

Statistics

qPCR values were obtained from three independent crude lysate productions and two independent gradient-purified AAV productions. The luciferase data shown were attained by three biological replicates for crude lysate experiments and two biological replicates for purified AAV experiments. For every biological replicate, three technical replicates were performed. All error bars indicate the standard error of the mean (SEM). The differences between DJ and all other capsid variants were tested for statistical significance by the Anderson–Darling many-to-one comparison test followed by a Benjamini–Hochberg correction. *P*-values <0.05 were considered statistically significant ($^*P < 0.05$; $^{**}P < 0.01$; $^{***}P < 0.001$). All *P*-values are listed in Supplementary Tables S2–S5. Statistical analysis was performed in R (version 4.3.2).

Results

Vector design of nanobody insertions into the AAV-DJ capsid for FAP-mediated cell targeting

To enhance the infection efficacy of AAV specifically for FAP receptor-positive cells, but not FAP receptor-negative cells, we inserted a FAP nanobody into the capsid of AAV-DJ (Figure 1A). We chose in total eight different insertion positions on the capsid surface: three positions in the 2/5-fold wall (Q259, N262 and Q387), two positions in the protruding pore (N328 and N337), two positions in the depression around the pore (N664 and S670) and the previously proven insertion position T456 at the tip of the 3-fold protrusion (Figure 1B) (19,20). Since VP3 makes up the majority of the AAV capsid, we restricted the nanobody embeddings to VP1 or VP2, thereby avoiding potential steric hindrance of capsid formation by too many nanobodies on a single capsid. For insertions into VP1 only, the start codons for VP2 (T138A) and VP3 (M203K, M211L and M235L) were mutated prior to introducing the FAP nanobody. Further, we generated a rep2–capDJ plasmid with a mutated start codon of VP1 (M1K), complementing VP2 and VP3 expression during AAV production. Likewise, a VP2-only plasmid by mutating start codons of VP1 and VP3 was generated, as well as a plasmid providing only VP1 and VP3 by mutating the VP2 start codon (Figure 1C). For the nanobody insertions, we chose two different types of linkers: one short, symmetric linker pair (SGGGG on both sides) and an asymmetric linker pair, with a long N-terminal 5xSGGGG linker and a short C-terminal GGGGS linker, which was previously used by Eichhoff *et al.* for their nanobody insertions into VR4 (19). To interrogate AAV retargeting in the context of adding targeting nanobodies to the AAV capsid alone, we initially did not mutate AAV-DJ's HBD (R587–590), which is often done to attenuate capsid binding to heparan sulfate proteoglycans (HSPGs). Altogether, a total of 32 FAP nanobody variants were generated: 8 positions × 2 different VPs × 2 linker sets.

FAP nanobody insertions boost transduction in FAP receptor-positive cells

All variants, as well as an AAV-DJ control and controls for the split VP expression plasmids (VP1 and VP2/3 or VP2 and VP1/3 expressed from separate plasmids), were produced as crude lysates packaging a CAG promoter-driven NanoLuc payload. Post-production, titers were assessed by qPCR. We found that none of the variants had titers statistically significantly different from the AAV-DJ control. However, we noted a trend that almost invariably all VP1 insertion variants resulted in higher titers than AAV-DJ (Supplementary Figure S2). Next, we used these crude lysates to infect the human prostate cancer cell line R1 at an MOI of 1×10^3 vg/cell, which is FAP receptor negative as verified by flow cytometry (Supplementary Figure S3A–C). Forty-eight hours post-transduction, a luciferase assay using furimazine substrate for the NanoLuc was conducted and photon counts were normalized to the AAV-DJ control (Figure 2A). All VP2 insertion variants and nearly all VP1 insertion variants infected R1 cells less efficiently than the AAV-DJ parent (Figure 2A), indicating that the nanobody insertions to some extent negatively impact the uptake and intracellular processing of the AAV. To test our hypothesis that FAP nanobody insertions into the AAV capsid can boost infection of FAP receptor-positive cells, the same AAV samples were used to infect R1-FAP cells, which stably expressed the human FAP receptor (Supplementary Figure S3D). We found that insertions into positions N262, N328, Q387, T456, N664 and S670 surpassed the infection potency of AAV-DJ, independent of the linker type and whether the FAP nanobody insertion was made into VP1 or VP2. The best variant, VP2-N262-asymmetric, infected R1-FAP cells even ~8-fold better than AAV-DJ. Conversely, insertions into positions Q259 and N337 did not enhance infection and showed an equal infection reduction as seen for the assay with the FAP receptor-negative R1 cells (Figure 2B). We calculated a FAP nanobody-mediated specificity gain as the ratio of off- to on-target infection efficacy (R1-FAP/R1 infectivity normalized to AAV-DJ). By this metric, our data reveal an up to ~18-fold improved infection in R1 than in R1-FAP cells for the VP2-N262-asymmetric variant. Even all other variants, which were able to mediate a FAP nanobody-specific infection in R1-FAP cells, showed a specificity gain of >4-fold (Figure 2C). Lowering the dose of transduced AAV to 5×10^2 and 1×10^2 vg/cell showed comparable results, demonstrating that the specificity gain is dose independent (Supplementary Figure S4). Since the R1-FAP cell line is engineered to overexpress FAP, we turned our attention to a cell line with lower endogenous expression (compared to R1-FAP), such as the melanoma cell line SK-MEL-24 (Supplementary Figure S3E). For the infection of SK-MEL-24 cells, the same trend of infection gain was observed. Not only the symmetric VP1 insertion at position T456 stands out with a 5-fold infection increase, but also VP2 insertions at positions N262, N328, T456 and N664 surpassed the AAV-DJ infection potency by at least 2-fold (Figure 2D). To test whether the observed specificity gains are truly FAP nanobody specific, we performed two control experiments. First, we confirmed the binding of the FAP nanobody to the human FAP protein with a pulldown experiment. We immobilized a recombinant human FAP protein with a biotin tag to streptavidin magnetic beads and subsequently incubated with either AAV-DJ or a nanobody insertion variant (Supplementary Figure S5A). Most capsid variants containing the FAP nanobody insertion were efficiently pulled down, whereas the AAV-DJ control was not. The variant with an insertion at position N337 also had low pulldown efficiency (only 6.7%; Supplementary Figure S5B). Notably, this vari-
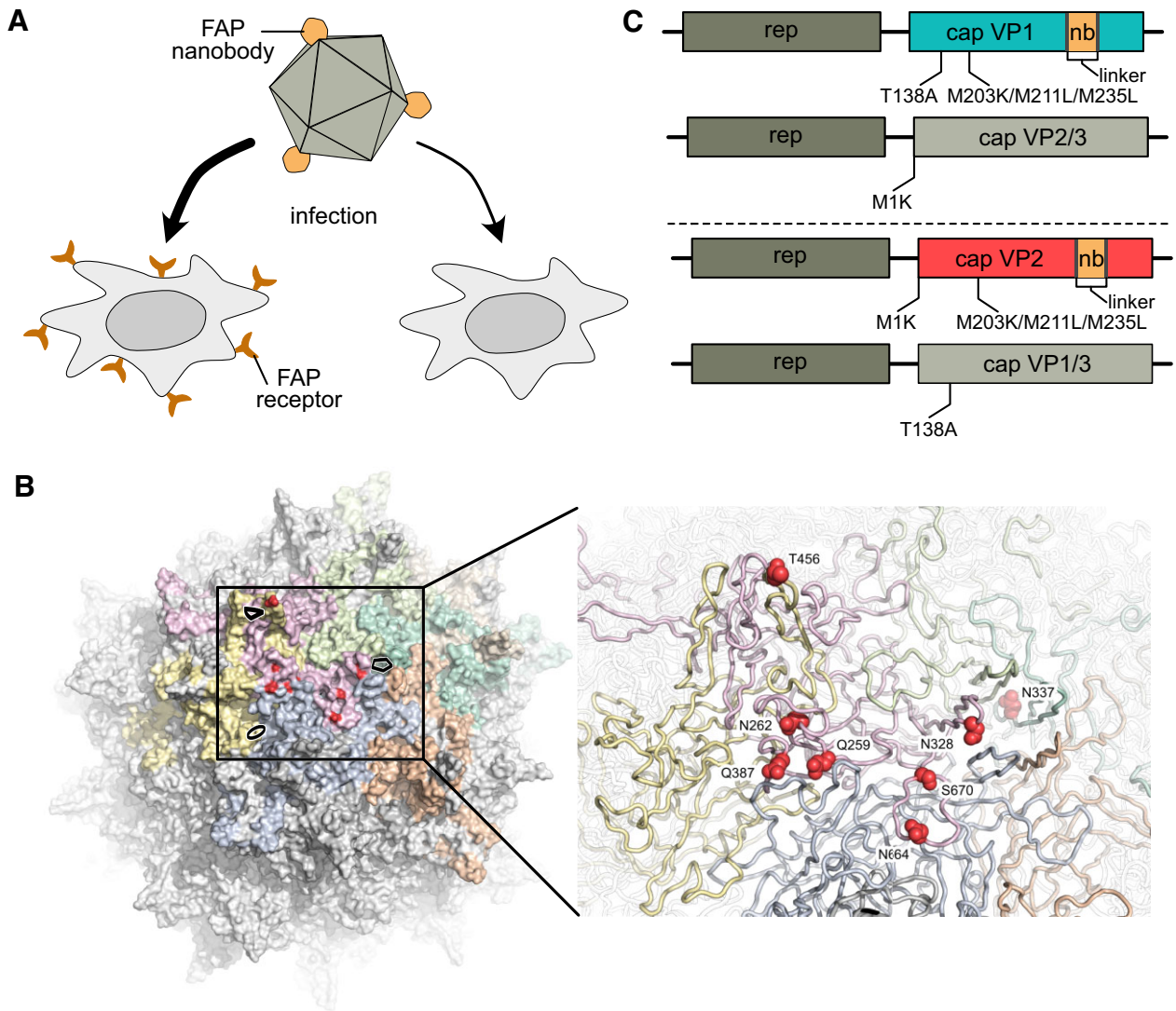
Figure 1. FAP nanobody incorporation at different positions of AAV-DJ. (**A**) Schematic of enhanced infection of FAP receptor-positive cells compared to FAP receptor-negative cells by incorporating a FAP nanobody into the AAV capsid. (**B**) AAV-DJ capsid structure (RCSB PDB 7KFR) from the outside (left) with a zoom-in (right). The eight FAP nanobody insertion positions are labeled. (**C**) Plasmid design of nanobody (nb) insertion into either VP1 (top) or VP2 (bottom) and the respective *trans*-complementation plasmids for AAV production.

ant also failed to mediate an infection boost in FAP receptor-positive cells (Figure 2B–D). As a second control, we used an isotype control experiment with a GFP nanobody. To this end, two variants (VP1-T456 and VP1-N664, both with symmetric linkers) were produced and tested in a one-on-one comparison to their FAP nanobody counterparts. As expected, there was no GFP nanobody-specific infection gain as seen for the FAP nanobody (Supplementary Figure S6).

Comparison of infection gain from different cell types reveals the most robust nanobody insertion positions

The differences and similarities between the two different cell lines tested, R1-FAP and SK-MEL-24, are illustrated in Figure 3A. Overall, FAP nanobody embedding into VP2 yielded a higher infection rate on average than into VP1, except for position T456, the previously published benchmark (19). This position seemed to tolerate nanobody insertions irrespective of the linker. Similarly good to position T456 functioned the

variants with insertion at positions N262, N328 and N664, showing the most robust infection gains (Figure 3A). No infection gain was observed in either cell line for embeddings into positions Q259 and N337. Mapping averaged infection gains for each insertion position into VP1 or VP2 onto the capsid structure revealed no apparent tolerability configuration with regard to the different interfaces of the AAV capsid. For example, all three positions located close to each other within the 2/5-fold wall (Q259, N262 and Q387) reached very different nanobody-mediated infection gains (Figure 3B,C).

Elimination of the HBD further restricts infection to FAP receptor-positive cells

HSPGs are known cell surface receptors used by AAV for cell entry. They are bound by the HBD motif (RGNR), which is found on many capsid serotypes, including AAV-DJ (32–34). Since HSPG is highly abundant on hepatocytes, it is assumed that the HSPG–HBD interaction is the main driver of the predominant liver tropism of AAV-DJ (35) and other serotypes.
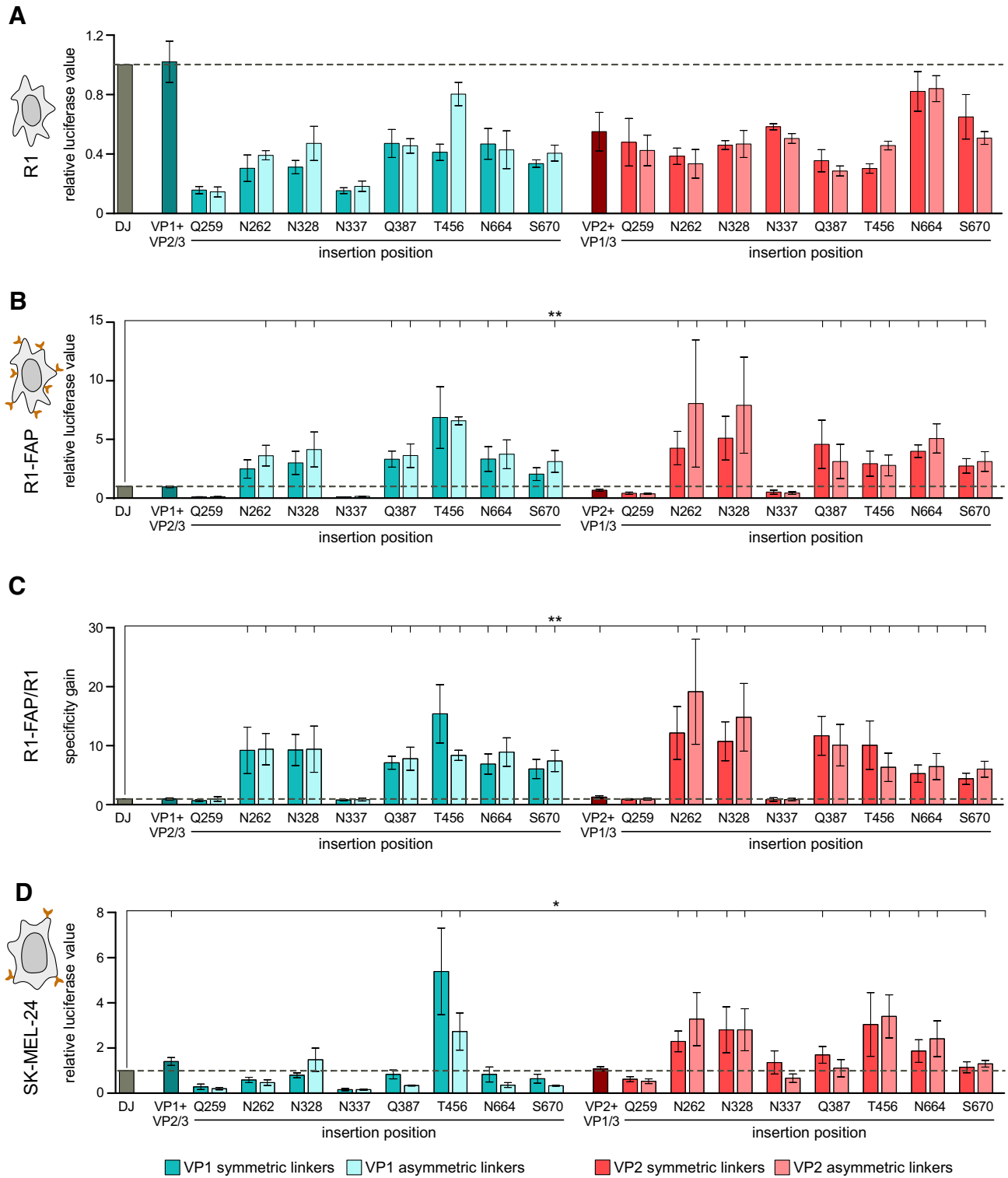
Figure 2. FAP nanobody incorporation at various positions enhances infection of FAP receptor-positive cells. R1 (**A**), R1-FAP (**B**) and SK-MEL-24 (**D**) cells were transduced at an MOI of 1×10^3 vg/cell with the indicated capsid variants, followed by a luciferase assay. Photon counts were normalized to the AAV-DJ controls. (**C**) Relative luciferase values from panels (A) and (B) were divided by each other to calculate the specificity gain. (A–D) The dashed horizontal line highlights the AAV-DJ control level. Data are means ± SEM. $^{*}P < 0.05$ and $^{**}P < 0.01$ by the Anderson–Darling many-to-one comparison test followed by a Benjamini–Hochberg correction.

A

B

VP1 insertion infectivity gain

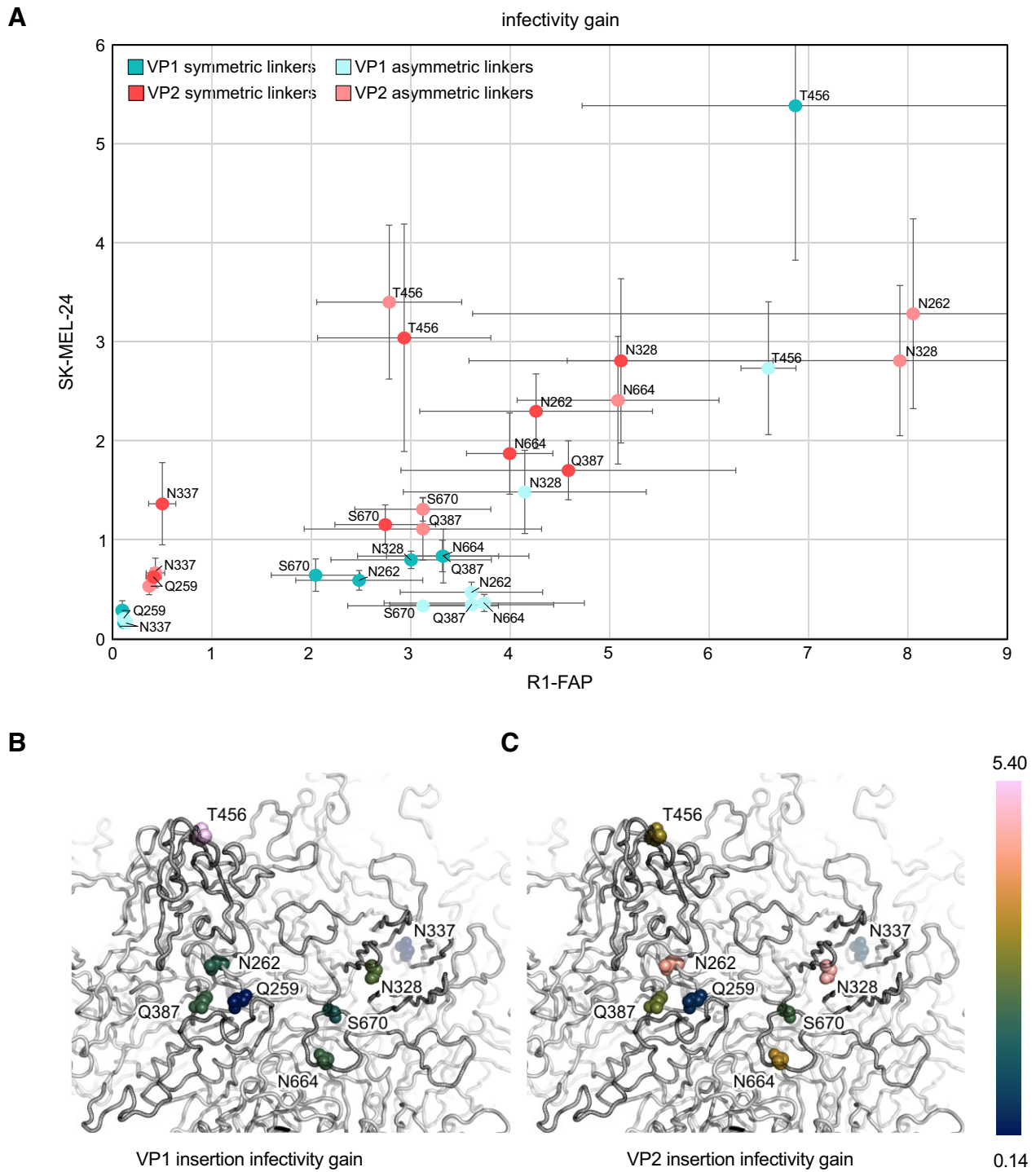**C**

VP2 insertion infectivity gain

Figure 3. Comparison of infection gain between R1-FAP and SK-MEL-24 cells. (**A**) Scatter plot representing the specificity gain of FAP nanobody insertion variants in R1-FAP cells compared to SK-MEL-24 cells. Data are means ± SEM. Averaged infectivity gains determined in R1-FAP and SK-MEL-24 cells from both linker types for FAP nanobody insertion into VP1 (**B**) and VP2 (**C**) were mapped onto the AAV-DJ capsid structure (RCSB PDB 7KFR).

Initially, we left the HBD in place to show that FAP nanobody insertion can overcome the natural HBD-mediated binding to FAP receptor-positive cells. However, in an *in vivo* context, these engineered capsids would still infect off-target cell types with abundant HSPGs, such as liver cells, to a high degree. We thus proceeded with eliminating the HBD by mutating the two arginines of the HBD motif to alanines (R587A and R590A) of our AAV-DJ control, one of our best FAP insertion vari-

ants (VP2-N328-asymmetric) and a variant that showed no FAP-specific infection boost (VP2-N337-asymmetric). These three variants alongside the AAV-DJ control were produced as iodixanol gradient-purified virus and titers were quantified by qPCR. While AAV-DJ without HBD produced equally well as the AAV-DJ control, the two FAP nanobody insertion variants gave ~2× lower titers (Supplementary Figure S7). Just as in our luciferase assays with crude lysates, we infected R1,

R1-FAP and SK-MEL-24 cells at an MOI of 1×10^3 vg/cell, followed by a luciferase activity assay as a measure of infection potency (Figure 4A–C). While R1 cells that were infected by the AAV-DJ control showed a strong luciferase signal, the signal from all three variants without HBD was reduced by more than two orders of magnitude (Figure 4A). In contrast, in the R1-FAP cells, variant VP2-N382-asymmetric without HBD was able to rescue the luciferase signal almost up to the level of the AAV-DJ control, unlike AAV-DJ without HBD and VP2-N377-asymmetric without HBD (Figure 4B). In SK-MEL-24 cells, with a low abundance of the FAP receptor, the rescue by VP2-N382-asymmetric without HBD was, as we expected, less pronounced (Figure 4C). Since the liver shows by far the strongest infection of all organs by AAV-DJ (35), we also tested our variants without HBD in hepatocytes, representing an off-target cell type. We chose the hepatocellular carcinoma cell line, HepG2, which we confirmed to be FAP receptor negative by flow cytometry (Supplementary Figure S3F). While the AAV-DJ control potently infected the HepG2 cells, all three variants without HBD showed a reduced luciferase signal by more than two orders of magnitude, as observed for the R1 off-target cells (Figure 4D). Capsid engineering that combines a FAP nanobody insertion with HBD elimination is thus rendering the AAV capsid highly specific for FAP receptor-positive cells.

Discussion

AAV has been proven to be a suitable vector to efficiently deliver transgenes for cell and gene therapies (1). Nonetheless, broad tissue tropism of natural serotypes hampers its applicability whenever a cell-type-specific targeting is of interest. Different capsid engineering approaches have been applied to tackle this issue, including peptide display (9–14), the recovery of AAV ancestors (36) and the insertion of domains with retargeting abilities (17,18,37). In particular, the embedding of nanobodies into the AAV capsid has been strikingly successful in boosting a cell-specific transduction (19,20).

Nanobodies naturally come with outstanding properties. They are small (15 kDa) and stable, and have antibody-like binding affinities and, on top, a low immunogenicity (38). Previous studies had successfully incorporated ARTC2.2, P2X7, CD38, CD4 and GFP nanobodies into VR4 of VP1 and subsequently showed a nanobody-specific uptake by cells expressing the cognate receptor (18–20). Based on our prior domain insertional profiling screen (22), we postulated that nanobodies can be embedded throughout the capsid's surface, instead of only into the 3-fold protrusion (VR4). Additional options for nanobody insertions may potentially synergize existing VR4 engineering approaches.

In this study, we incorporated a FAP nanobody into eight different positions, covering different surface areas of AAV-DJ. The benchmark position T456, which is part of VR4, was included as a reference. As hypothesized, we could show that AAV capsids can harbor nanobody insertions at various locations, including the 2-fold valley and the protruding 5-fold pore. None of the tested variants showed a reduction in production titer (Supplementary Figure S2) and six out of the eight chosen positions were able to mediate a FAP receptor-specific infection boost of up to ∼18-fold (Figure 2). The two different linker pairs tested had very minor influence on whether an insertion variant boosted infection or not

(Figure 2), which is surprising regarding the fact that the two termini of a nanobody are ∼40 Å apart and the short symmetric linker could cause sheering forces to the capsid. The choice which VP protein was engineered made a bigger difference. We observed increased production titers for almost all VP1 variants, whereas VP2 insertions produced similar to the AAV-DJ parent when produced as crude lysate (Supplementary Figure S2). Despite higher production titers, nanobody incorporations into VP1 had a lower transduction efficacy compared to VP2 insertions (Figures 2 and 3). We speculate that this effect is caused by a reduced incorporation rate of VP1–nanobody monomers. It has been shown that VP1 is indispensable for the infection process. The unique N-terminus, also known as VP1u, lies inside the capsid and comprises a phospholipase domain (PLA2) as well as a nuclear localization signal. Both play a critical role in endosomal escape and nuclear entry, respectively (39–42). On the one hand, if the capsid contains fewer VP1 monomers, fewer VP1u overhangs occupy the inner cavity of the capsid, possibly facilitating the more efficient packaging of the DNA cargo. On the other hand, fewer VP1 monomers also result in a reduced infection potency. Consequently, the VP2 monomer, for which no crucial functions are known, appears to be the better choice for nanobody insertions. While Eichhoff *et al.* only tested a single insertion into VP1, Hamann *et al.* also tested N-terminal fusions of a nanobody to VP2, which was less effective than the known VR4 insertion position of VP1 (19,20). Supporting the notion that engineering VP2 is the more promising route, a previous study by us also tested VP2 insertions into VR4 and found that this insertion was superior compared to the VP1 equivalent (18).

Overall, our FAP nanobody insertion into six out of the eight positions (N262, N328, Q387, T456, N664 and S670) resulted in an infection boost in FAP receptor-positive cells (Figure 2). All these positions have in common that they are on the surface of the capsid, but they are located at very different regions, i.e. at the 5-fold pore (N328), 3-fold protrusion (T456), 2/5-fold wall (N262 and Q387) and valley surrounding the pore (N664 and S670; Figure 3B and C). One could argue that four of these are part of known VRs and therefore more likely to tolerate insertions (N262 is part of VR1, N328 is part of VR2, Q387 is part of VR3 and T456 is part of VR4), but N664 and S670 also showed a receptor-specific infection and these two positions are neither part of a VR nor a general protrusion (8). Further, three of the positions amenable to nanobody insertions (N262, Q387, T456) are known to play a role in the binding of the ubiquitously used AAVR receptor (43,44). We speculate that insertions right behind these residues are likely to block the AAVR binding and instead promote the FAP receptor binding. Another important receptor used by AAV is HSPG, which is bound by the HBD (R587–R590) of the capsid. Previous studies had removed this binding domain prior to inserting the nanobody to achieve a null-tropism capsid parent to which the infection potency was compared (18–20). We could show here that even after leaving this known receptor binding site in place, a nanobody-mediated infection boost for on-target cells occurred. Importantly, when we eliminated the HBD domain in addition to FAP nanobody insertion, we achieved a strong reduction of infection in hepatocytes, while maintaining infection potency for FAP receptor-positive cells (Figure 4). Considering hepatotoxicity to be a common adverse effect in AAV clinical trials (45), reduced infection of liver cells—to which
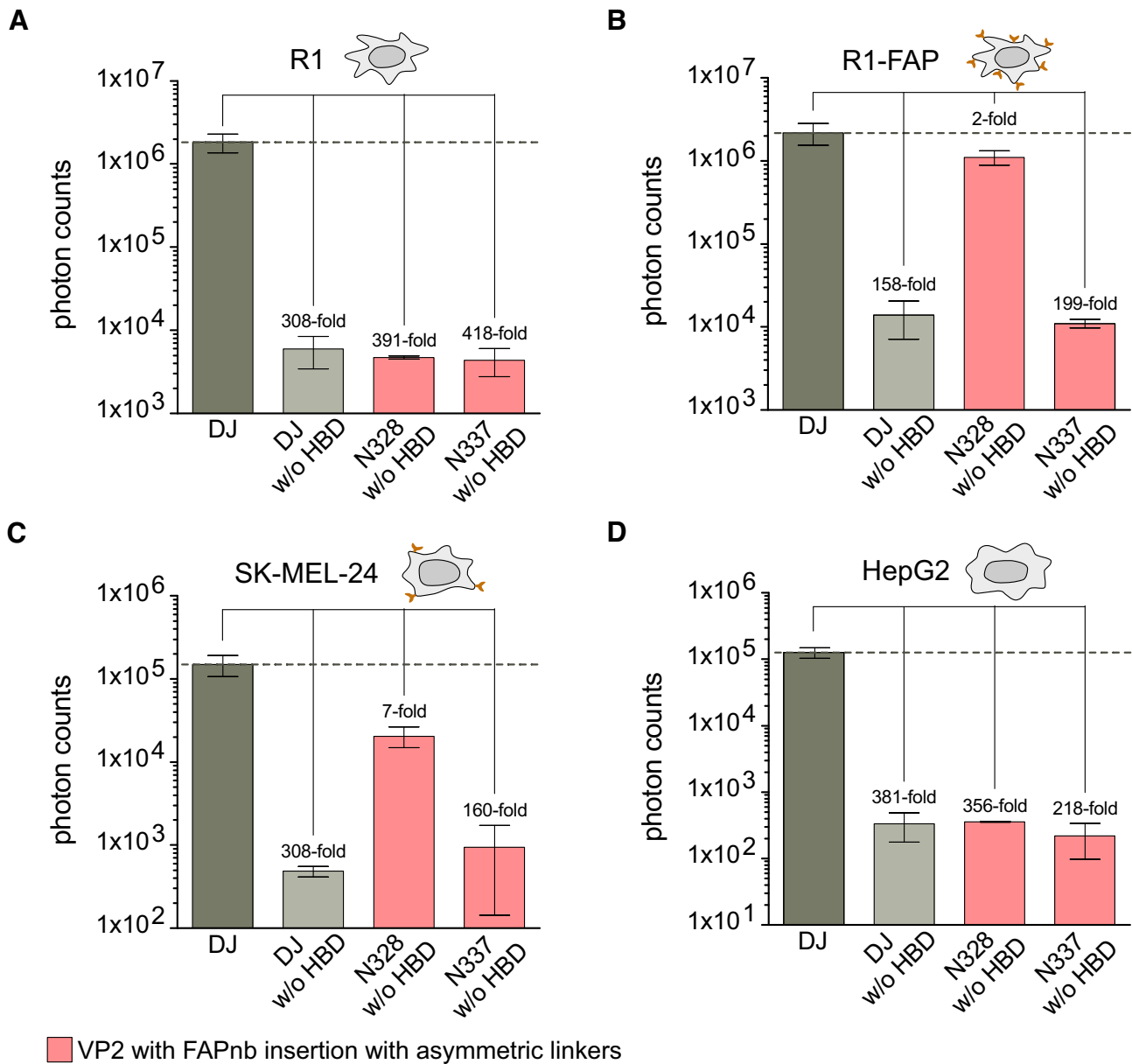
Figure 4. Infection potency of FAP nanobody insertion variants tested on different cell lines. R1 (**A**), R1-FAP (**B**), SK-MEL-24 (**C**) and HepG2 (**D**) cells were transduced at an MOI of 1×10^3 vg/cell with the indicated capsid variants, followed by a luciferase assay. The dashed horizontal line highlights the AAV-DJ control level. Data are means of two replicates ± SEM.

AAV-DJ has strong tropism—is highly significant when engineering nanobody–AAV for *in vivo* applications.

Two insertion positions that we tested, N337 and Q259, did not result in any infection gain, although their packaging was not impaired (Figure 2 and Supplementary Figure S2). N337 is partly hidden within the pore and an insertion there could potentially block the externalization of VP1u through the pore during infection. Q259 lies within the 2/5-fold wall closely abutting a neighboring VP subunit (unlike the nearby N262). Prior work has shown that interfacial dynamics at the 2-fold axis play a role in externalization of VP1u during infection, which may explain the lack of infectivity of insertion variant at this position (46).

Although we only used AAV-DJ as a test bed, our data for position T456 align with reports of nanobody insertions into AAV-2 VP1 (19), which suggests generalizability to other serotypes, especially to those that share sequence similarities at the 2-fold and 5-fold interfaces. The FAP nanobody used in this study can be used to direct AAV to cancer or cancer-associated cells with a high FAP expression profile (23), but further experiments *in vivo* are required for validation. Notably, the straightforward replacement of the GFP nanobody in our previous study (22) with a FAP nanobody here suggests that nanobody swapping at the 2-fold valley and 5-fold axis hotspots is a viable strategy to rapidly diversify AAV tropism. With more and more nanobodies being developed, the here demonstrated tolerability of nanobody insertions at various locations within the AAV capsid can further expand the applicability of nanobody-directed cell-specific targeting.

Data availability

All plasmids are available upon request. Flow cytometry data are available on FlowRepository (Repository ID: FR-FCM-Z789).

Supplementary data

Supplementary Data are available at NARMME Online.

Acknowledgements

Funding

Conflict of interest statement

None declared.

References

1. Wang,D., Tai,P.W.L. and Gao,G. (2019) Adeno-associated virus vector as a platform for gene therapy delivery. *Nat. Rev. Drug Discov.*, **18**, 358–378.
2. Jay,F.T., Laughlin,C.A. and Carter,B.J. (1981) Eukaryotic translational control: adeno-associated virus protein synthesis is affected by a mutation in the adenovirus DNA-binding protein. *Proc. Natl Acad. Sci. U.S.A.*, **78**, 2927–2931.
3. Srivastava,A., Lusby,E.W. and Berns,K.I. (1983) Nucleotide sequence and organization of the adeno-associated virus 2 genome. *J. Virol.*, **45**, 555–564.
4. Johnson,F.B., Ozer,H.L. and Hoggan,M.D. (1971) Structural proteins of adenovirus-associated virus type 3. *J. Virol.*, **8**, 860–863.
5. Rose,J.A., Maizel,J.V., Inman,J.K. and Shatkin,A.J. (1971) Structural proteins of adenovirus-associated viruses. *J. Virol.*, **8**, 766–770.
6. Snijder,J., van de Waterbeemd,M., Damoc,E., Denisov,E., Grinfeld,D., Bennett,A., Agbandje-McKenna,M., Makarov,A. and Heck,A.J. (2014) Defining the stoichiometry and cargo load of viral and bacterial nanoparticles by Orbitrap mass spectrometry. *J. Am. Chem. Soc.*, **136**, 7295–7299.
7. Xie,Q., Bu,W., Bhatia,S., Hare,J., Somasundaram,T., Azzi,A. and Chapman,M.S. (2002) The atomic structure of adeno-associated virus (AAV-2), a vector for human gene therapy. *Proc. Natl Acad. Sci. U.S.A.*, **99**, 10405–10410.
8. Govindasamy,L., Padron,E., McKenna,R., Muzyczka,N., Kaludov,N., Chiorini,J.A. and Agbandje-McKenna,M. (2006) Structurally mapping the diverse phenotype of adeno-associated virus serotype 4. *J. Virol.*, **80**, 11556–11570.
9. Tse,L.V., Klinc,K.A., Madigan,V.J., Castellanos Rivera,R.M., Wells,L.F., Havlik,L.P., Smith,J.K., Agbandje-McKenna,M. and Asokan,A. (2017) Structure-guided evolution of antigenically distinct adeno-associated virus variants for immune evasion. *Proc. Natl Acad. Sci. U.S.A.*, **114**, E4812–E4821.
10. Chan,K.Y., Jang,M.J., Yoo,B.B., Greenbaum,A., Ravi,N., Wu,W.L., Sánchez-Guardado,L., Lois,C., Mazmanian,S.K., Deverman,B.E., et al. (2017) Engineered AAVs for efficient noninvasive gene delivery to the central and peripheral nervous systems. *Nat. Neurosci.*, **20**, 1172–1179.
11. Dalkara,D., Byrne,L.C., Klimczak,R.R., Visel,M., Yin,L., Merigan,W.H., Flannery,J.G. and Schaffer,D.V. (2013) *In vivo*-directed evolution of a new adeno-associated virus for therapeutic outer retinal gene delivery from the vitreous. *Sci. Transl. Med.*, **5**, 189ra76.
12. Deverman,B.E., Pravdo,P.L., Simpson,B.P., Kumar,S.R., Chan,K.Y., Banerjee,A., Wu,W.L., Yang,B., Huber,N., Pasca,S.P., et al. (2016) Cre-dependent selection yields AAV variants for widespread gene transfer to the adult brain. *Nat. Biotechnol.*, **34**, 204–209.
13. Körbelin,J., Sieber,T., Michelfelder,S., Lunding,L., Spies,E., Hunger,A., Alawi,M., Rapti,K., Indenbirken,D., Müller,O.J., et al. (2016) Pulmonary targeting of adeno-associated viral vectors by next-generation sequencing-guided screening of random capsid displayed peptide libraries. *Mol. Ther.*, **24**, 1050–1061.
14. Tabebordbar,M., Lagerborg,K.A., Stanton,A., King,E.M., Ye,S., Tellez,L., Krunnfusz,A., Tavakoli,S., Widrick,J.J., Messemer,K.A., et al. (2021) Directed evolution of a family of AAV capsid variants enabling potent muscle-directed gene delivery across species. *Cell*, **184**, 4919–4938.
15. Weinmann,J., Weis,S., Sippel,J., Tulalamba,W., Remes,A., El Andari,J., Herrmann,A.K., Pham,Q.H., Borowski,C., Hille,S., et al. (2020) Identification of a myotropic AAV by massively parallel *in vivo* evaluation of barcoded capsid variants. *Nat. Commun.*, **11**, 5432.
16. Judd,J., Wei,F., Nguyen,P.Q., Tartaglia,L.J., Agbandje-McKenna,M., Silberg,J.J. and Suh,J. (2012) Random insertion of mCherry into VP3 domain of adeno-associated virus yields fluorescent capsids with no loss of infectivity. *Mol. Ther. Nucleic Acids*, **1**, e54.
17. Michels,A., Frank,A.M., Günther,D.M., Mataei,M., Börner,K., Grimm,D., Hartmann,J. and Buchholz,C.J. (2021) Lentiviral and adeno-associated vectors efficiently transduce mouse T lymphocytes when targeted to murine CD8. *Mol. Ther. Methods Clin. Dev.*, **23**, 334–347.
18. Zdechlik,A.C., He,Y., Aird,E.J., Gordon,W.R. and Schmidt,D. (2020) Programmable assembly of adeno-associated virus–antibody composites for receptor-mediated gene delivery. *Bioconjug. Chem.*, **31**, 1093–1106.
19. Eichhoff,A.M., Börner,K., Albrecht,B., Schäfer,W., Baum,N., Haag,F., Körbelin,J., Trepel,M., Braren,I., Grimm,D., et al. (2019) Nanobody-enhanced targeting of AAV gene therapy vectors. *Mol. Ther. Methods Clin. Dev.*, **15**, 211–220.
20. Hamann,M.V., Beschorner,N., Vu,X.K., Hauber,I., Lange,U.C., Traenkle,B., Kaiser,P.D., Foth,D., Schneider,C., Büning,H., et al. (2021) Improved targeting of human CD4+ T cells by nanobody-modified AAV2 gene therapy vectors. *PLoS One*, **16**, e0261269.
21. Bao,G., Tang,M., Zhao,J. and Zhu,X. (2021) Nanobody: a promising toolkit for molecular imaging and disease therapy. *EJNMMI Res.*, **11**, 6.
22. Hoffmann,M.D., Zdechlik,A.C., He,Y., Nedrud,D., Aslanidi,G., Gordon,W. and Schmidt,D. (2023) Multiparametric domain insertional profiling of adeno-associated virus VP1. *Mol. Ther. Methods Clin. Dev.*, **31**, 101143.
23. Garin-Chesa,P., Old,L.J. and Rettig,W.J. (1990) Cell surface glycoprotein of reactive stromal fibroblasts as a potential antibody target in human epithelial cancers. *Proc. Natl Acad. Sci. U.S.A.*, **87**, 7235–7239.
24. Hintz,H.M., Cowan,A.E., Shapovalova,M. and LeBeau,A.M. (2019) Development of a cross-reactive monoclonal antibody for detecting the tumor stroma. *Bioconjug. Chem.*, **30**, 1466–1476.

25. Xin,L., Gao,J., Zheng,Z., Chen,Y., Lv,S., Zhao,Z., Yu,C., Yang,X. and Zhang,R. (2021) Fibroblast activation protein-α as a target in the bench-to-bedside diagnosis and treatment of tumors: a narrative review. *Front. Oncol.*, **11**, 648187.

26. Engler,C., Kandzia,R. and Marillonnet,S. (2008) A one pot, one step, precision cloning method with high throughput capability. *PLoS One*, **3**, e3647.

27. Rothbauer,U., Zolghadr,K., Tillib,S., Nowak,D., Schermelleh,L., Gahl,A., Backmann,N., Conrath,K., Muyldermans,S., Cardoso,M.C., *et al.* (2006) Targeting and tracing antigens in live cells with fluorescent nanobodies. *Nat. Methods*, **3**, 887–889.

28. Hintz,H.M., Gallant,J.P., Vander Griend,D.J., Coleman,I.M., Nelson,P.S. and LeBeau,A.M. (2020) Imaging fibroblast activation protein alpha improves diagnosis of metastatic prostate cancer with positron emission tomography. *Clin. Cancer Res.*, **26**, 4882–4891.

29. Grieger,J.C., Choi,V.W. and Samulski,R.J. (2006) Production and characterization of adeno-associated viral vectors. *Nat. Protoc.*, **1**, 1412–1428.

30. Zolotukhin,S., Byrne,B.J., Mason,E., Zolotukhin,I., Potter,M., Chesnut,K., Summerford,C., Samulski,R.J. and Muzyczka,N. (1999) Recombinant adeno-associated virus purification using novel methods improves infectious titer and yield. *Gene Ther.*, **6**, 973–985.

31. Hall,M.P., Unch,J., Binkowski,B.F., Valley,M.P., Butler,B.L., Wood,M.G., Otto,P., Zimmerman,K., Vidugiris,G., Machleidt,T., *et al.* (2012) Engineered luciferase reporter from a deep sea shrimp utilizing a novel imidazopyrazinone substrate. *ACS Chem. Biol.*, **7**, 1848–1857.

32. Mietzsch,M., Broecker,F., Reinhardt,A., Seeberger,P.H. and Heilbronn,R. (2014) Differential adeno-associated virus serotype-specific interaction patterns with synthetic heparins and other glycans. *J. Virol.*, **88**, 2991–3003.

33. Opie,S.R., Warrington,K.H., Agbandje-McKenna,M., Zolotukhin,S. and Muzyczka,N. (2003) Identification of amino acid residues in the capsid proteins of adeno-associated virus type 2 that contribute to heparan sulfate proteoglycan binding. *J. Virol.*, **77**, 6995–7006.

34. Summerford,C. and Samulski,R.J. (1998) Membrane-associated heparan sulfate proteoglycan is a receptor for adeno-associated virus type 2 virions. *J. Virol.*, **72**, 1438–1445.

35. Grimm,D., Lee,J.S., Wang,L., Desai,T., Akache,B., Storm,T.A. and Kay,M.A. (2008) *In vitro* and *in vivo* gene therapy vector evolution via multispecies interbreeding and retargeting of adeno-associated viruses. *J. Virol.*, **82**, 5887–5911.

36. Zinn,E., Pacouret,S., Khaychuk,V., Turunen,H.T., Carvalho,L.S., Andres-Mateos,E., Shah,S., Shelke,R., Maurer,A.C., Plovie,E., *et al.* (2015) *In silico* reconstruction of the viral evolutionary lineage yields a potent gene therapy vector. *Cell Rep.*, **12**, 1056–1068.

37. Münch,R.C., Muth,A., Muik,A., Friedel,T., Schmatz,J., Dreier,B., Trkola,A., Plückthun,A., Büning,H. and Buchholz,C.J. (2015) Off-target-free gene delivery by affinity-purified receptor-targeted viral vectors. *Nat. Commun.*, **6**, 6246.

38. Muyldermans,S. (2013) Nanobodies: natural single-domain antibodies. *Annu. Rev. Biochem.*, **82**, 775–797.

39. Grieger,J.C., Snowdy,S. and Samulski,R.J. (2006) Separate basic region motifs within the adeno-associated virus capsid proteins are essential for infectivity and assembly. *J. Virol.*, **80**, 5199–5210.

40. Kronenberg,S., Böttcher,B., von der Lieth,C.W., Bleker,S. and Kleinschmidt,J.A. (2005) A conformational change in the adeno-associated virus type 2 capsid leads to the exposure of hidden VP1 N termini. *J. Virol.*, **79**, 5296–5303.

41. Nam,H.J., Gurda,B.L., McKenna,R., Potter,M., Byrne,B., Salganik,M., Muzyczka,N. and Agbandje-McKenna,M. (2011) Structural studies of adeno-associated virus serotype 8 capsid transitions associated with endosomal trafficking. *J. Virol.*, **85**, 11791–11799.

42. Venkatakrishnan,B., Yarbrough,J., Domsic,J., Bennett,A., Bothner,B., Kozyreva,O.G., Samulski,R.J., Muzyczka,N., McKenna,R. and Agbandje-McKenna,M. (2013) Structure and dynamics of adeno-associated virus serotype 1 VP1-unique N-terminal domain and its role in capsid trafficking. *J. Virol.*, **87**, 4974–4984.

43. Xu,G., Zhang,R., Li,H., Yin,K., Ma,X. and Lou,Z. (2022) Structural basis for the neurotropic AAV9 and the engineered AAVPHP.eB recognition with cellular receptors. *Mol. Ther. Methods Clin. Dev.*, **26**, 52–60.

44. Zhang,R., Cao,L., Cui,M., Sun,Z., Hu,M., Zhang,R., Stuart,W., Zhao,X., Yang,Z., Li,X., *et al.* (2019) Adeno-associated virus 2 bound to its cellular receptor AAVR. *Nat. Microbiol.*, **4**, 675–682.

45. Asokan,A. and Shen,S. (2023) Redirecting AAV vectors to extrahepatic tissues. *Mol. Ther.*, **31**, 3371–3375.

46. Horowitz,E.D., Finn,M.G. and Asokan,A. (2012) Tyrosine cross-linking reveals interfacial dynamics in adeno-associated viral capsids during infection. *ACS Chem. Biol.*, **7**, 1059–1066.